Targeting metabolic adaptations in the breast cancer–liver metastatic niche using dietary approaches to improve endocrine therapy efficacy

Qianying Zuo[1], Ayca Nazli Mogol[2], Yu-Jeh Liu[1], Ashlie Santaliz Casiano[2], Christine Chien[3], Jenny Drnevich[4],Ozan Berk Imir[2], Eylem Kulkoyluoglu-Cotul[1], Nicole Hwajin Park[1], David J Shapiro[5,6], Ben Ho Park[7], Yvonne Ziegler[8], Benita S. Katzenellenbogen[6,8], Evelyn Aranda[9], John D. O'Neill[9], Akshara Singareeka Raghavendra[10], Debu Tripathy[10], Zeynep Madak Erdogan[1,2,3,6,11, 12]

[1] Department of Food Science and Human Nutrition, University of Illinois at Urbana-Champaign, Urbana, IL 61801

[2] Division of Nutritional Sciences, University of Illinois at Urbana-Champaign, Urbana, IL 61801

[3] Carle Illinois College of Medicine, University of Illinois at Urbana-Champaign, Urbana, IL 61801

[4] Roy J. Carver, Biotechnology Center, University of Illinois at Urbana-Champaign, Urbana, IL 61801

[5] Department of Biochemistry, University of Illinois at Urbana-Champaign, Urbana, IL 61801

[6] Cancer Center at Illinois, Urbana, IL 61801

[7] Vanderbilt University Medical Center, Nashville, TN 37232

[8] Department of Molecular and Integrative Physiology, University of Illinois at Urbana-Champaign, Urbana, IL 61801

[9] Xylyx Bio, Inc., Brooklyn, NY 11226

[10] Department of Breast Medical Oncology, MD Anderson Cancer Center, Houston, TX 77030

[11] Beckman Institute for Advanced Science and Technology, Urbana, IL 61801

[12] Carl R. Woese Institute of Genomic Biology, Urbana IL, 61801

ZME is funded by an investigator-initiated grant from Karyopharm Therapeutics. ZME is a consultant for GSK. ZME is Editor-in-chief for Endocrine and Metabolic Science. BSK has ownership interest in Celcuity, Inc. BHP is a paid consultant for Hologic, EQRx, Jackson Laboratories, Sermonix and is a paid scientific advisory board member with ownership interest for Celcuity. Under separate licensing agreements between Horizon Discovery, LTD and The Johns Hopkins University, BHP is entitled to a share of royalties received by the University on sales of products. The terms of this arrangement are being managed by the Johns Hopkins University in accordance with its conflict of interest policies. The other authors declare that they have no conflict of interest.

Corresponding author:

Zeynep Madak Erdogan

Email: zmadake2@illinois.edu

Phone: 12173009063

Abstract

Estrogen receptor-positive (ER^+) metastatic tumors contribute to nearly 70% of breast cancer-related deaths. Most patients with ER^+ metastatic breast cancer (MBC) undergo treatment with the estrogen receptor agonist fulvestrant (Fulv) as standard of care. Yet, among such patients, metastasis in liver is associated with reduced overall survival compared to other metastasis sites. The factors underlying the reduced responsiveness of liver metastases to ER agonists remain unknown, impeding the development of more effective treatment approaches to improve outcomes for patients with ER^+ liver metastases. We therefore evaluated site-specific changes in MBC cells and determined the mechanisms through which the liver metastatic niche specifically influences ER^+ tumor metabolism and drug resistance. We characterized ER activity of MBC cells both in vitro, using a novel system of tissue-specific extracellular matrix hydrogels representing the stroma of ER^+ tumor metastatic sites (liver, lung and bone), and in vivo, in liver and lung metastasis mouse models. ER^+ metastatic liver tumors and MBC cells grown in liver hydrogels displayed upregulated expression of glucose metabolism enzymes in response to Fulv. Furthermore, differential ERα activity, but not expression, was detected in liver hydrogels. In vivo, increased glucose metabolism led to increased glycogen deposition in liver metastatic tumors, while a fasting-mimicking diet increased efficacy of Fulv treatment to reduce the metastatic burden. Our findings identify a novel mechanism of endocrine resistance driven by the liver tumor microenvironment. These results may guide the development of dietary strategies to circumvent drug resistance in liver metastasis, with potential applicability in other metastatic diseases.

Introduction

About one-third of women with early-diagnosed non-metastatic breast cancer later develop metastatic disease [1], and 90% of breast cancer deaths result from metastases that is intractable to treatment [2, 3]. Among US women with breast cancer, an estimated 168,000 had metastatic breast cancer (MBC) in 2020 [4]. This condition confers poor outcomes, with a median survival of approximately 18–24 months from metastatic tumor diagnosis [5]. These adverse outcomes underscore the need to identify mechanisms promoting metastatic disease and treatment resistance.

MBC commonly spreads to the liver [6, 7]. Importantly, patients with liver metastasis (40.8%) have significantly increased death risk, similar to brain metastasis, and a disproportionally higher mortality rate compared to lung (36.8 %) or bone metastases (67%) [8-11]. About 70% of metastatic tumors express estrogen receptor alpha (ERα), rendering MBC responsive to endocrine-based therapies such as Fulvestrant (Fulv) [12, 13]. This ERα antagonist is the only clinically approved selective ER degrader prescribed either alone or in combination with CDK4/6 or PI3K inhibitors (for PIK3CA mutant tumors) to treat MBC, independent of metastatic site. Notably, patients with liver metastases have poorer response to Fulv compared to patients with bone or lung metastases [6, 7, 14]. Left untreated, survival for patients with MBC in liver is typically 4–8 months [15]. For those receiving endocrine/biotherapy or chemotherapy, median times to progression are in the range of 20–30 months with initial therapy, and these times shorten progressively with subsequent treatments until clinical resistance develops [10]. Therefore, there is a critical need for novel therapeutic approaches that will provide a durable therapy response or cure for patients with ER^+ liver MBC.

Metastatic tumor phenotypes and treatment responses result from complex interactions between tumor cells and components of the tumor microenvironment, including inflammatory cells, fibroblasts, and biochemical composition and physical properties of the extracellular matrix [16]. A crucial aspect of this microenvironment is the metabolic state. Cancer cells exhibit a remarkable metabolic plasticity [17, 18], whereby they adapt to new metastatic environments by rewiring their metabolic pathways [16]. Yet, these changes not only provide building blocks to sustain the cells' biological functions, they also create novel vulnerabilities that are potentially exploitable through pharmacological or dietary interventions.

We recently showed that MBC cells grown in tissue-specific extracellular matrix hydrogels to tune their microenvironment displayed altered metabolic profiles that rendered the cells vulnerable to metabolic inhibitors; notably, treatment with these inhibitors improved MBC cell responses to endocrine therapy [19]. Previous work using syngeneic mouse models showed metastatic site-specific metabolic adaptations in ER-negative breast tumors [20, 21]. Yet, the impact of the liver microenvironment on ER^+ MBC cell metabolic reprogramming and response to ER-targeting agents is unknown.

Here, we sought to identify how the metabolism–cancer nexus in liver affects the response of metastatic ER^+ tumors to Fulv, focusing particularly on tumor-intrinsic metabolic mechanisms arising following Fulv exposure. Spatial and bulk transcriptomic, and metabolic analysis of MBC cells and in vivo xenograft tumors identified an upregulation of glucose metabolism in the liver niche in response to Fulv. We fed mice with diets with differing carbohydrate levels to modulate metastatic burden and improve Fulv responses. Our findings delineating the underlying causes of the unique MBC

response to Fulv in the liver should inform the design of future clinical trials to test efficacy of combining dietary interventions with endocrine therapies to improve treatment response.

Materials and Methods

Clinical Data and Analysis

The breast cancer management database at The University of Texas MD Anderson Cancer Center was used to identify patients for the current study, with the following inclusion criteria: age ≥ 18 years, diagnosed with de novo or recurrent $ER^+/HER2^-$ MBC between 1997 and 2021, with metastasis to the liver and receipt of Fulv in their metastatic setting. To evaluate the difference in overall mortality among patients with MBC to the liver, we analyzed 3388 patients with MBC in a MD Anderson Cancer Center cohort study. Patients with either primary or secondary liver metastasis were identified as having hepatic involvement. All other patients with MBC were identified as having non-liver metastasis. Kaplan-Meier methods were used to visualize overall survival and survival after metastasis. The Cox proportional hazards model was then used to compare the survival between patients with metastasis to the liver versus metastasis to other sites. These models were adjusted for age at diagnosis, BMI, race, and tumor stage.

Cell Culture

All cell lines were obtained from American Type Culture Collection (Manassas, VA) unless indicated otherwise. MCF7 (ATCC HTB-22) (RRID:CVCL_0031) and T47D (ATCC HTB-133) (RRID:CVCL_0553) parental cells were cultured in RPMI-1640 medium with NEAA salts (Sigma, St Louis, MO, USA), 5% fetal bovine serum (FBS)

(HyClone, Logan, UT), 100 µg/mL penicillin/streptomycin (Invitrogen, Carlsbad, CA, USA) and 50 mg/mL Gentamicin (Gibco, Gaithersburg, MD). MCF7/*ESR1*^{D537S} and -*ESR1*^{Y537S} cells (RRID:CVCL_0031-citation needed) were generated as described in [22] and were cultured in Dulbecco's Modified Eagle Medium (DMEM) with NEAA salts, 10% FBS, 100 µg/mL penicillin/streptomycin, and 50 mg/mL gentamicin. T47D *ESR1*^{D537S} and T47D *ESR1*^{Y537S} cells (RRID: CVCL_0553-citation needed) were cultured in Modified Eagle Medium (MEM) with NEAA salts, 10% FBS, 100 µg/mL penicillin/streptomycin, and 50 mg/mL gentamicin. Cell line authentication was performed by checking activity and expression of ERα, proliferative responses to ER agonists and antagonists for all cell lines, and sequencing of MCF7/*ESR1*^{Y537S} and MCF7/*ESR1*^{D537G} as described [23].

3-D Cell Culture Models

IN SITE Metastasis Kit (Xylyx Bio, Inc., NY) containing TissueSpec Bone (MTSBN101), Liver (MTSLV101), and Lung (MTSLG101) ECM Hydrogels, were used to model tumor microenvironments according to the manufacturer's protocol. Briefly, 2×10^3 cells were encapsulated in corresponding extracellular matrix (ECM) hydrogels by mixing them with tissue culture matrix. A mixture volume of 100 uL/well was placed in 96-well plates in triplicate. Plates were incubated at 37°C in a humidified environment with 5% CO_2 for at least 45 minutes to achieve gelation. Cells were treated with media containing Veh or 1µM Fulv every Monday and Friday for three weeks. Oncosphere formations were visualized by Invitrogen EVOS XL Core Light Microscope (4X and 25X magnifications) (Waltham, MA, USA). OpenCFU colony counting software (http://opencfu.sourceforge.net/) was used to automatically count colony number and

size. All statistical analyses were completed by using GraphPad Prism 8 software (RRID:SCR_002798).

Western Blot

Western blot analysis used specific antibodies against β-actin (Sigma Aldrich, St. Louis) and ERα (F10, Santa Cruz Biotechnology, Santa Cruz, CA). MCF-7 cells were seeded at 2–4x10^5 cells in 10-cm dishes in 5 mL growth media. The next day, cells were treated with fresh media and collected 15 min later into 250 µL lysis buffers. Cell lysate was prepared using RIPA buffer. Samples were sonicated three times for 10 s to shear the DNA. Ten micrograms of protein were loaded onto 10% SDS gels. Primary antibodies were used at 1:500 except for β-actin (1:5,000). Secondary antibodies are from Licor biosciences (Goat anti rabbit IRDdye 800 and goat anti mouse IRDye 680). Proteins were visualized using Odyssey LI-COR Imaging System that detect infrared dye on the secondary antibodies.

In Vivo Xenograft Study

Four-week-old, ovariectomized, NOD SCID gamma (NSG) immunodeficient female mice were obtained from The Jackson Laboratory (Bar Harbor, ME). All experiments involving animals were conducted in accordance with National Institutes of Health standards for the use and care of animals, with protocols approved by the University of Illinois at Urbana-Champaign (UIUC; IACUC protocol #20158). After one week of acclimatization to the housing facility, we injected 1×10^6 MCF7-ESR1^{Y537S} cells resuspended in 1% PBS via tail vein and randomized animals to indicated treatment groups. Mice were housed in 12-h light-dark cycle.

Diet and metastatic burden study: Three different diets were implemented for this study: Control (F4031, Bioserv, Flemington, NJ), High-fat Diet (HFD) (F3282, Bioserv), and Fasting-mimicking Diet (FMD) (F3666, Bioserv) (**Supplementary Table 1**). We randomized N=8 mice to one of the two treatments Vehicle (Veh) or Fulv in each diet group. Fulv (Sigma) was dissolved in 10% DMSO and 90% corn oil and administrated via intramuscular injection (100 mg/kg) twice a week (Monday, Friday) for four weeks.

FMD and Fulv response study: In our diet studies using MCF7 ESR1^{Y537S} cells, metastatic tumor bioluminescence radiance had an average of 1.9X10^{6} p/sec/cm^{2}/sr and standard deviation of 1.5X10^{6} p/sec/cm^{2}/sr. Based on these values and Type 1 error of 5% and Type II error of 5%, to observe a significant tumor response, 8 mice per group were randomized to the Fulv treatment or control groups (i.e., Control/Veh; Control/Fulv; FMD/Veh; FMD/Fulv). Fulv was dissolved in 10% DMSO and 90% corn oil and administrated via intramuscular injection (100 mg/kg) twice a week (Monday, Friday) for four weeks.

For all experiments, food intake and body weight were measured twice weekly for the study duration. After six weeks of treatment, mice were euthanized, and organs were harvested. Tumor growth was monitored over time using an in vivo bioluminescence imaging (IVIS) system (PerkinElmer). Tumor burden was assessed and measured (final metastatic tumor nodules) at necropsy. Aliquots of the samples were either flash frozen, frozen in RNAlater (Thermo Scientific, Waltham, MA, USA) for RNA isolation, or crosslinked in 10% neutral buffered formalin at room temperature (Millipore Sigma, Burlington, MA) for histological analysis.

Histology

Tissues were cut in 5-micron sections using a microtome (Leica RM1255, Austria). For ERα immunostainings, tissues were deparaffinized and hydrated through graded alcohols to water. Antigen retrieval was performed by using citrate buffer, pH 6.0 in a steamer for 1 hour. Samples were blocked in hydrogen peroxide for 10 min. To remove non-specific protein staining, samples were blocked with Background buster (Innovex Biosciences, Richmond, CA) for 10 min and rinsed with TBS-Tween solution, pH 7.6. Then, samples were incubated with anti-ERα (F10, Santa Cruz Biotech) (RRID: AB_631470) primary antibody overnight at 4° C. After rinsing with TBS-Tween solution, pH 7.6, samples were stained with secondary anti-rabbit and anti-mouse HRP-Polymer (Biocare Medical, Concord, CA) for 30 min. Finally, samples were incubated with DAB (Innovex, Richmond, CA) for 5 min and counterstained with hematoxylin, dehydrated, and mounted on slides. Visualization of samples was performed with Nanozoomer Slide Scanner (Hamamatsu, Japan) at 80X magnification, and positive staining quantification was performed using NDP software.

For the Periodic Acid Schiff's (PAS) staining, paraffin sections were deparaffinized in xylene and rehydrated through graded alcohols to water. Then they were placed in 0.5 % periotic acid for ten minutes. After rinsing well in water, they were placed in McManus Schiff's Reagent (Newcomer Supply, Inc., Middleton, Wisconsin) for 10 minutes. Following a 30 second rinse in 0.55 % Potassium Metabisulfite, the slides were placed in warm running tap water for10 minutes. They were then counterstained with modified Harris hematoxylin (Thermo Fisher Scientific, Kalamazoo, MI). They were then dehydrated, cleared in xylene and mounted. For glycogen digestion, following

deparaffinization, the slides were placed in 1% amylase in a 37 degree incubator for 30 minutes before proceeding with the PAS stain.

Gene Expression Analysis

To identify gene sets regulated in different ECMs, *S*elective *E*strogen *R*eceptor *M*odulators (SERM), or by Fulv in liver metastatic tumors, RNASeq analysis was performed. For hydrogel experiments, 30-mm cell culture plates were coated with Native Coat ECMs for liver, lung, or bone (Xylyx). Then, these plates were incubated at 37ºC in a humidified environment with 5% CO_2 for at least for 1 hour. MCF7-ESR1^{Y537S} cells were seeded on coated plates after removing native coat mixtures at a density of 2×10^3 cells/well in DMEM. Cell lysates were collected using Trizol after 24 h of culture. MCF7-ESR1^{Y537S} cells were treated with Vehicle (Veh, 0.5% EtOH), 10^{-6} M 4-hydroxytamoxifen (4OHT) (Sigma), 10^{-6} M Fulv (Sigma), or 10^{-6} M Palbociclib (Palb) (Sigma) for 24 h. Concentrations of drugs were selected are based on our previously published studies [19, 24] and clinical data [25-27]. Experiments were performed in triplicate. For cell line xenograft tumors of MCF7-ESR1^{Y537S} cells, Veh- or Fulv-treated tumors were homogenized in 1 mL of TRIzol reagent (Life Technologies, Carlsbad, CA, USA). Total RNA was extracted with TRIzol reagent according to the manufacturer's protocol and cleaned using a kit (QIAGEN, Hilden, Germany). RNA quality was assessed using bioanalyzer. Total RNA from each sample (three per treatment group) was sequenced at the UIUC sequencing center, and data were generated in Fastqc file format to compare transcript abundance between the four treatment groups.

Preprocessing and quality control: Fastqc files containing raw RNA sequencing data were trimmed using Trimmomatic (Version 0.38) (RRID:SCR_011848) [28]. Next, the

reads were mapped to the human reference genome (GRCh37) or mouse reference genome (GRCm38) from the Ensembl (RRID:SCR_002344) [29] database and aligned using the STAR alignment tool (RRID:SCR_015899) (Version 2.7.0f) [30]. Read counts were generated from SUBREAD (Version 1.6.3) (RRID:SCR_009803) [31], and feature counts were exported for statistical analysis in R. Quality control and normalization was conducted in R using edgeR (Version 3.24.3) (RRID:SCR_012802) [32]. Statistical analysis was conducted in R using limma (Version 3.38.3) (RRID:SCR_010943) [33, 34]. Empirical Bayesian statistics were conducted on the fitted model of the contrast matrix. Differentially expressed genes were then determined by fold-change and p-value with Benjamini and Hochberg multiple test correction for each gene, for each treatment relative to the vehicle control. We considered genes with fold-change >1.5 and p-value <0.05 as statistically significant, differentially expressed. Cluster3 software was used for clustering the differentially expressed genes. Data were visualized using Treeview Java. Principal components analysis (PCA) was performed using StrandNGS (Version 3.1.1). Gene set enrichment analysis (GSEA, RRID:SCR_003199) [35, 36] was used to identify GO terms associated with different treatments.

Visium Spatial transcriptomics libraries are constructed in the at the Carl R. Woese Institute for Genomic Biology Core Facility and the DNA Services laboratory of the Carver Biotechnology Center at the University of Illinois at Urbana-Champaign. Briefly, frozen tissues were sectioned and placed onto a Tissue Optimization Slide with eight capture areas, each having thousands of spots with poly-dT capture probes. Tissue sections were permeabilized across a time-course from 3 to 30 minutes. The mRNAs from the tissue anneal to the oligos, were converted to cDNA by reverse

transcription with a fluorophore and the sections were evaluated with the Zeiss Axio Observer Z1 microscope. The permeabilization condition producing the brightest image with the least diffusion were chosen for the processing of the tissues. A permeabilization time of 12 minutes was selected for these samples. Next, tissue sections were placed onto the Visium spatial Gene Expression slide, which contains 4 capture area squares 6.5mm x 6.5mm. Each square has approximately 5,000 spots with barcoded poly-dT oligos. Tissue sections were fixed, stained with hematoxylin and eosin (H&E) and visualized with the Hananatsu Nanozoomer microscope. After permeabilization, messenger RNAs were converted into spatially-barcoded cDNAs following the 10x Genomics protocol. The double-stranded-barcoded cDNAs are then denatured and converted into a sequencing-ready, dual-indexed libraries. The final libraries were quantitated on Qubit and the average size determined on the AATI Fragment Analyzer (Advanced Analytics, Ames, IA), then diluted to 5nM concentration and further quantitated by qPCR on a Bio-Rad CFX Connect Real-Time System (Bio-Rad Laboratories, Inc. CA). The libraries were pooled by qPCR value and capture spot coverage and sequenced on an Illumina NovaSeq 6000 to a length of 28nt (read 1, contains the spot barcode and unique molecular identifier used for removing PCR duplicates), 10nt for each index (libraries contain unique dual indexes to prevent index switching) and 150nt for read 2 (the cDNA read) to a minimum depth of at least 100,000 cDNA read 2 per spot. Fastq.gz files were generated and demultiplexed with SpaceRanger 1.3.0. Data was processed and visualized using Space Ranger Analysis Pipelines and Loupe browser using a combined human (GRCh38) and mouse (GRCm39) reference based on Ensembl Release 104. Visium uses the cDNA barcodes

to associate the transcripts to an X-Y coordinate on the slide, which can then be used to overlay the H&E-stained image with the transcript information from a spatial viewpoint. The R package Seurat was used to read in both the count data and the images. To identify spots that were primarily mouse host, we calculated the proportion of all UMIs that were from human genes and excluded spots that were <= 25% human. All mouse genes were also removed and then all 4 samples were normalized together using sctransform, then principal components analysis was performed and the top 30 PCs were used in both nearest neighbor cluster calling and UMAP dimension reduction.

Metabolomics Analysis

MCF7-ESR1^{Y537S} cells were seeded at a density of 2x10^5 cells/plate in the same coated plates after removing native coat mixtures as explained above. After 24 hours, metabolites were extracted using acetonitrile/isopropanol/water and stored at -80ºC until submitted to the Metabolomics Center in the Roy J Carver Biotechnology Center at UIUC. GC/MS whole metabolite profiling was performed to detect and quantify the metabolites by using gas chromatography-mass spectrometry (GC/MS) analysis. Metabolite profiles were acquired using an Agilent GC-MS system (Agilent 7890 gas chromatograph, an Agilent 5975 MSD, and an HP 7683B autosampler). Spectra of all chromatogram peaks were evaluated using the AMDIS 2.71 and a custom-built database with 460 unique metabolites. All known artificial peaks were identified and removed before data mining. To allow comparison between samples, all data were normalized to the internal standard in each chromatogram. This analysis identifies about 200 metabolites and reports a relative abundance of metabolites, which enabled us to compare metabolites across the sample batch. Metabolomics data with sample class

annotations (No ECM, Liver ECM) were uploaded to the Statistical Analysis tool of MetaboAnalyst software (RRID:SCR_015539) version 4.0 [37]. Features with more than 50% missing values were removed. Data were normalized based on values from No ECM samples. Data were log transformed and scaled using the auto-scaling feature. A heatmap of class averages of 25 metabolites was generated using the Heatmap feature with default options for clustering and restricting the data to top 25 metabolites ranked by t-test. Partial least squares discriminant analysis (PLS-DA) was performed to sharpen the separation between No ECM and Liver ECM groups to distinguish metabolic profiles. VIP scores for the top 25 metabolites that discriminated between treatment groups were calculated and displayed using the PLS-DA tool. Fold-change analysis was performed to compare the absolute value of change of metabolites between two group means. Enrichment analysis and pathway analysis were used to identify metabolic pathways associated with enriched metabolites (fold change >2 or <0.05).

Seahorse Metabolic Profiling Assays

Seahorse XFp plates were coated with Native Coat ECMs for bone, lung, or liver (Xylyx). The coated plates were incubated at 37°C in a humidified environment with 5% CO_2 for at least for 1 hour. Cells were seeded in the coated Seahorse plates after removing native coat mixtures. MCF7-ESR1^{Y537S} cells were seeded at a density of 3×10^4 in corresponding treatment media without phenol red in each well of the XFp Cell Culture miniplates, respectively (Seahorse Bioscience Inc., Billerica, MA, USA). The next day, the cartridges were hydrated with the calibration solution and kept in a non-CO_2 incubator at 37°C overnight. In parallel, a duplicate of each plate was used for cell

counting to monitor cell number changes after 24 h of treatments, and Seahorse data were normalized to total cell number. On the assay day, cells were washed with XF Base Media without phenol red (Seahorse Bioscience Inc., Santa Clara, CA) supplemented with 10 mM L-glucose, 2 mM L-glutamine (Gibco), and 1 mM sodium pyruvate (Gibco, Waltham, MA). The ECAR (mpH/min) and OCR (pmol/min) values were obtained by using Seahorse XFp Cell Energy Phenotype Test Kit (Seahorse Bioscience Inc.), which were run with Seahorse XFp Analyzer (Seahorse Bioscience Inc.). Experiments were performed in triplicate and repeated at least three times.

ChIP-seq Analysis

ChIP-seq analysis was performed as described previously using MCF7-*ESR1*^{Y537S} cells [38, 39]. ERα–DNA or IgG–DNA complexes were immunoprecipitated using ERα-specific F10 and HC20 antibodies (Santa Cruz Biotech, 3:100 dilution). ChIP DNA was obtained from three pooled biological replicates. Libraries were prepared according to Illumina Solexa ChIP-Seq sample processing (San Diego, CA), and single-read sequencing was performed using the Illumina HiSeq 2000. Sequences generated were mapped uniquely onto the human genome (hg18) by Bowtie2 (RRID:SCR_016368). The MACS (model-based analysis of ChIP-seq) algorithm was used to identify enriched peak regions (default settings) with a P value cutoff of 6.0e−7 and FDR of 0.01, as we have described [40, 41].

Statistical Analyses

Data from all studies were analyzed using a one-way analysis of variance (ANOVA) to compare different ligand effects, or a two-way-ANOVA model to compare time-dependent changes. All datasets were tested for normal distribution. Normally

distributed data were analyzed using unpaired t-tests with a Bonferroni correction to identify treatments that produced significantly different results (* $p < 0.05$, ** $p < 0.01$, *** $p < 0.001$, **** $p < 0.0001$). For every main effect that was statistically significant at $\alpha = 0.05$, pairwise t-tests were conducted to determine which ligand treatment levels significantly differed. For these t-tests, the Bonferroni correction was employed to control experiment-wise type I error rate at $\alpha = 0.05$ followed by Bonferroni post hoc test. Data that were not normally distributed were analyzed using Mann-Whitney test for nonparametric data (* $p < 0.05$, ** $p < 0.01$, *** $p < 0.0001$). Statistical significance was calculated using GraphPad Prism 9 for Windows.

Data Availability

Gene expression data were submitted to the GEO database and will be available from the day of the acceptance of the manuscript.

Results

Patients with liver metastatic breast tumors respond poorly to Fulv

Small cohort studies reported that patients with liver metastases are less responsive to Fulv compared to patients with bone or lung metastases [6, 7, 14]. To validate these findings in a larger cohort, we analyzed data from an ongoing trial for patients with ER^+ MBC. We identified 1556 (46%) patients in our cohort with liver metastasis. Median overall survival in patients with liver metastasis was 10 years (9.6, 10.4), which was significantly shorter than those with metastasis elsewhere. The hazard ratio was 1.46 (1.34, 1.59), indicating an increased risk of mortality associated with liver metastasis across all treatment regimens (**Fig.1A**). Those with liver metastasis also had worse survival post-metastasis, with a median survival of 6.7 years (6.5, 7.0) compared

to 5.8 years (5.6, 6.0) in the non-liver metastasis cohort (**Fig.1B**). To characterize ER antagonist responses of MBC cells and test potential efficacy of combination therapies, we previously used decellularized hydrogels from different metastatic tissues [19]. To examine the differences in Fulv response when MBC cells are grown in different hydrogels, we used MCF7-ESR1^{Y537S} cells (**Fig. 1C**). Estrogen receptor alpha gene (*ESR1*) mutations were identified in 15-40% of patients with ER^{+} metastatic tumors [42-45]. Since these ESR1-activating mutations within the ligand-binding domain of ERα are enriched only in metastatic tumors [42-45], particularly in visceral tissue metastasis including liver metastases [46-48], we used this cell line to model MBC cell behavior in response to metastatic niche. Consistent with the clinical observation, MBC cells grown on liver hydrogels were less responsive to Fulv compared to cells grown on Matrigel or lung or bone hydrogels (**Fig. 1D and Figure S1**).

ER^{+} MBC cells display distinct transcriptomes and ER cistromes in different tissue-specific ECM hydrogels

To determine the molecular changes associated with different metastatic environments, we compared gene expression profiles from MCF7-ESR1^{Y537S} cells grown on plastic (2D), bone, liver, or lung ECM hydrogels. MBC cells grown on different hydrogels exhibited distinct gene expression profiles (**Fig. 2A and 2B**). Intriguingly, gene sets associated with classical ERα target genes were downregulated in liver but not in bone or lung hydrogels (**Fig. 2C**), despite a lack of change in ERα mRNA or protein expression (**Fig. 2D**). To investigate why classical ERα target genes were downregulated on liver hydrogels, we performed ChIP-seq analysis, which revealed that ERα recruitment to chromatin was significantly altered in a niche-specific manner (**Fig.**

2E). For example, ER binding sites in cluster 2 (C2), present in cells grown in 2D plastic or bone hydrogels, were lost in cells grown on liver or lung hydrogels. Overall, there were more ER binding sites in bone hydrogels compared to lung or liver (**Figure S2**). These binding sites mapped to classical ER target genes, consistent with **Fig. 2D.** A histogram for ERα binding to an example classical ERα target gene, GREB1, is shown in **Fig. 2F**. Conversely, a new cluster of binding sites, cluster 3 (C3), was present only in cells grown in liver hydrogels, indicating the liver metastatic niche can promote a distinct pattern of ERα recruitment. These binding sites mapped to genes involved in metabolic regulation and insulin signaling, suggesting that these newly gained sites might be responsible for an altered metabolic phenotype (**Table S2**). Moreover, the fraction of distal intergenic binding sites was increased in liver hydrogels compared to other sites (**Fig. 2G**). Estrogen response element was the most enriched motif in liver ER binding sites, suggesting a direct ERα binding to chromatin rather than tethering (**Table S3**).

Glucose dependence of MBC cells increases in liver hydrogels

To assess the impact of metastatic ECM on MBC metabolism, we grew MCF7-ESR1^{Y537S} cells on different ECMs. Growth of these cells on liver ECM caused an increase in both the glycolysis and oxidative respiration in Seahorse cell phenotype tests (**Fig. 3A**). To identify specific pathways impacted by liver ECM, we performed a metabolomic analysis. Growth of MBC cells on different hydrogels resulted in distinct metabolite profiles when a PLS-DA classification was performed (**Fig. 3B**). While the abundances of fatty acid and glucose metabolism pathway metabolites were increased on liver ECM, amino acid and nucleotide metabolism-related metabolites were increased on lung ECM (**Fig. 3C**). To dissect the specific fuel dependency on different

hydrogels, we assayed glycolytic and oxidative respiration, which showed that liver hydrogels but not hydrogels from bone or lung increased glycolytic respiration in the presence of full media, or media with glucose or pyruvate compared to cells that were grown on plastic (2D) (**Fig. 3D**). Liver ECM led to an increase in oxidative respiration only when cells were supplemented with full media (**Fig. 3E**). A Seahorse cell phenotype test in different media showed that MBC cells grown in media with glucose had an increase in glycolytic potential when also grown on liver ECM (**Fig. 3F**). Finally, we performed metabolomic profiling in MBC cells grown on liver ECM that were treated with Veh or Fulv. This analysis further showed that relative abundance of glucose metabolism-associated metabolites including pyruvate were increased in response to Fulv (**Fig. 3G**).

Glucose metabolism pathways are upregulated in liver metastatic tumors in vivo

To uncover the mechanistic basis of decreased Fulv efficacy in patients with ER^+ liver MBC, we used a preclinical xenograft mouse model with MCF7-$ESR1^{Y537S}$ cells. Tail vein injection of MCF7-$ESR1^{Y537S}$cells in NSG mice resulted in liver metastasis, with a small portion of tumors forming in the lung, and Fulv treatment failed to reduce metastatic burden (**Fig. 4A and 4B**). To study if metastatic site altered gene regulation in response to Fulv, we compared gene expression changes of MCF-7 $ESR1^{Y537S}$ liver and lung xenograft tumors. This analysis showed that Fulv reduced expression of classical ER target genes PgR and GREB1. However, unlike lung metastatic tumors, liver metastatic tumors failed to downregulate *GREB1* and *PCNA* in response to Fulv (**Fig. 4C**). To validate this observation, we performed spatial sequencing in Veh and

Fulv treated liver metastatic tumors. Overall, UMAP plots showed that tumors from same treatment groups clustered together (**Fig. 4D**). We identified 22 distinct clusters associated with liver metastatic tumors (**Fig.4E**). Human transcripts were majority of the transcripts identified in liver sections we analyzed (**Fig. 4F**). Interestingly, Fulv treatment increased ESR1 expression throughout the tumors. While MKI67 or PCNA expression did not change in response to Fulv, classical ER target changes GREB1, PgR and TSKU were downregulated (**Fig. 4G**). These results suggested that, while ERα retained some of its activity and Fulv response in liver metastatic tumors, suppression of cell proliferation in response to Fulv was lost.

Tumor metastatic burden correlates with carbohydrate levels in the diet

To determine why Fulv failed to reduce tumor progression and if any critical survival pathways were activated in response to Fulv, we performed RNASeq of liver metastatic tumors (**Fig. 5A**). Fulv significantly increased glycolysis and glycogenesis metabolism pathways, as well as lipid metabolism-related genes, consistent with our metabolomics analysis in **Fig. 3** (**Fig. 5B**). We compared changes in expression of genes in cells that were grown on plastic (2D) treated with Fulv, 4-hydroxytamoxifen, or palbociclib; different hydrogels (Bone, liver, or lung); or changes in mouse transcripts in xenograft tumors with Fulv treatments. We found that glycogen pathway regulation was strongest in xenograft samples, suggesting that glycogen pathway regulation occurs in liver MBC, but not when cells are treated with Fulv in 2D or even when cells were grown on liver hydrogels without other components of the tumor microenvironment (ECM) (**Fig. 5B**). Because we observed major metabolic and gene expression changes in glucose metabolism and an increased dependence on and utilization of glucose in models of

liver metastasis, we next tested the impact of different diets with varying carbohydrate contents in our MCF7-ESR1^{Y537S} xenograft model. Animals were provided with a Control diet, HFD, and FMD, which enabled us to examine impact of varying glucose or fat levels in the diet (**Table S1**). Metastatic burden was measured over 4 weeks (**Fig. 5C and 5D**). At the end of the experiment, livers from animals who consumed the FMD looked healthier and had less visible liver metastasis nodules (**Fig. 5E**). Throughout the study we also monitored animal weight and caloric intake. Using this data, we performed a correlation analysis using all the data we obtained from these measurements and diet composition data, which revealed that metastatic burden is positively correlated with carbohydrate levels, particularly with di- and polysaccharides, in the diet (**Fig. 5F**). This finding is consistent with our observation that there was an increased dependence on glucose metabolism in liver metastatic tumors (**Fig. 3**). We found that metastatic burden negatively correlated with fat intake levels, while no correlation was observed for protein levels in the diet (**Fig. 5F, Table S4**). Interestingly, PAS staining for glycogen revealed that in animals who were fed a control diet or HFD, glycogen deposition was primarily in tumors (**Fig. 5G**).

Targeting glycogen deposition using dietary approaches improve Fulv response of liver metastatic tumors

Because we observed major metabolic and gene expression changes in glucose and glycogen metabolism genes, and an increased dependence on and utilization of glucose in models of liver metastasis, we next tested the impact of an FMD on MCF7-ESR1^{Y537S} xenograft model. FMD prevents glycogen accumulation in the liver and thus blocks a glucose surge and resultant insulin release from the pancreas. In addition, a

recent study combining FMD with Fulv showed a reduced time to endocrine resistance in primary $ER^+/HER2^-$ mouse tumors and achieved complete response or stable disease in human patients [49]. To determine whether reducing glucose metabolism using an FMD might synergize with Fulv treatment in our in vivo liver metastasis model, we delivered MCF7-$ESR1^{Y537S}$ cells through tail vein injection in NSG mice. Consuming FMD synergized with Fulv treatment to reduce metastatic burden in mice with metastatic tumors (**Fig. 6A and 6B**) and decreased the number of visible metastatic nodules in the liver (**Fig. 6C and 6D**). Fulv treatment increased glycogen deposition in tumors (**Fig. 6E, column 3, and row 2**). These data provide proof of concept that combining a dietary intervention targeting glucose metabolism and glycogen deposition in liver provided a durable response to Fulv.

Discussion

Metastatic tumor phenotypes and responses to treatment reflect key aspects of the tumor microenvironment [50]. Here, we investigated tumor-intrinsic metabolic mechanisms that arise specifically in the liver metastatic niche. Using a combination of models, spatial and molecular data, and analytical methods, our findings reveal a key mechanism of endocrine resistance in liver MBC: niche-related metabolic plasticity in MBC cells that alters the response to ER-targeted therapies. This metastatic niche displays specific metabolic changes that provide a mechanistic basis for the poor success of Fulv treatment on survival of patients with ER^+ liver MBC. Yet, these changes also unveiled a unique metabolic vulnerability that could be exploited through dietary intervention to improve Fulv response.

Treatment of MBC in the clinic focuses on targeting mechanisms that underlie increased activity of selective cellular pathways. Indeed, interrogating and targeting signaling cascades in tumors has been fruitful in promoting the development of endocrine-based therapies combining CDK4/6 inhibitors, PI3K inhibitors, or mTOR pathway inhibitors with endocrine agents for ER^+ MBC [13]. Yet, none of these therapies is metastatic site-specific, and tumors can still develop resistance to combination therapies. In such cases, the cancer that develops is considerably more aggressive due to hyperactivation of compensatory pathways [51]. In contrast, we focused on inhibiting dynamic metabolic mechanisms enabling survival and therapy resistance in liver metastatic niches. Targeting metastatic site-specific metabolic vulnerabilities in ER^+ MBC is a novel approach and the impact of metabolic interventions on endocrine therapy effectiveness is underexplored.

To characterize ER antagonist responses of MBC cells and test potential efficacy of combination therapies, we previously used decellularized tissue-specific ECM hydrogels from different metastatic tissues [19]. Hydrogels constitute compatible niches to support ER^+ MBC growth and provide an opportunity to recapitulate metastatic site environment and analyze drug responses and metastasis-associated phenotypes in vitro. These commercial hydrogels are obtained from decellularized porcine tissues. Characterization of hydrogel composition by mass spectrometry and quantitative biochemical and biophysical assays showed that hydrogels retain tissue-characteristic ECM proteins as well as growth factors [19, 52, 53]. Scanning electron microscopy analysis revealed structural similarity to human tissues, and rheometry analysis showed conservation of biophysical properties of the hydrogels, such as stiffness and resistance

to deformation, as well as response of cancer cells grown in these matrices to drugs [19, 54]. We found that, consistent with the clinical observation, MBC cells grown on liver hydrogels were less responsive to Fulv compared to cells grown on Matrigel or lung or bone hydrogels. Supporting our observations in the hydrogel systems, an in vitro study reported reduced Fulv response when MCF7-ESR1^{Y537S} were cultured with human hepatocytes [55].

We observed altered ERα activity and recruitment in different tissue-specific ECM hydrogels. Since ERα expression is the same in different hydrogels, the altered ER recruitment pattern likely does not result from altered ER expression. Epigenetic marks are well established as a mechanism that dictates ERα recruitment to chromatin, target gene regulation, and response to ER antagonists [56-58]. Histone 3 displays altered acetylation at lysine 4, 9, and 27 in breast cancer cells that fail to respond to ER antagonists [58-60]. These results suggest an altered ERα activity in MBC cells residing in the liver microenvironment, and a role for metabolic and epigenetic enzymes to interact with ER in a Fulv-dependent manner to locally change epigenetic marks, which would lead to altered response to ERα antagonists. Future studies are needed to uncover these epigenetic differences based on metastatic sites.

Additionally, metastatic site adaptation [61, 62] and metabolic alterations in MBC cells result in epigenetic reprogramming due to changes in the availability of substrates for epigenetic enzymes [63-65]. Local acetyl-CoA production via recruitment of metabolic enzymes to chromatin enables coordination of environmental cues with histone acetylation and gene transcription, thus increasing fitness and survival of cancer cells in different metastatic tissues. Acetyl-CoA can be synthesized in the nucleus from

pyruvate by the pyruvate dehydrogenase complex (PDC) [66, 67], from acetate by acetyl-CoA synthetase 2 (ACSS2) [68, 69], or from citrate by ATP-citrate lyase (ACLY) [70]. Intriguingly, all these enzymes are upregulated in ER^+ liver metastatic tumors upon Fulv treatment, supporting a role for altered metabolism in changing tumors' epigenetic landscape.

Accumulating data indicate that practical clinical dietary intervention during cancer treatment has a profound impact in improving the efficacy of anticancer therapy, especially the FMD [71]. This diet is generally high-fat, moderate-protein, and very-low-carbohydrate, leading to a process known as ketogenesis [72]. Lipolysis-induced fatty acids are metabolized to acetoacetate, which is later converted to β-hydroxybutyrate (β-OHB) and acetone [73]. β-OHB is the most abundant ketone body derived from β-oxidation in the liver, and it replaces glucose as a primary source of energy [73]. Considering the impact of carbohydrates in promoting breast cancer cell proliferation, the FMD has the potential to limit or control tumor growth. Some animal studies support that an FMD inhibits not only the progression of the primary tumor but also systemic metastasis [74, 75]. By providing a low-glucose microenvironment, the FMD enhances the cancer cell therapeutic response through selective metabolic oxidative stress [76]. Recent evidence indicates that the combination of FMD with Fulv results in increased time to endocrine resistance in primary $ER^+/HER2^-$ mouse tumors and in complete response or stable disease in human patients [49]. This important study focused on the impact of FMD on circulating factors and signaling pathways; we instead focus on the impact of FMD on metabolic state of tumor cells. Recently, suppression of insulin feedback after PI3K inhibition using a FMD was proposed [77]. Our findings further

support use of this diet to improve endocrine therapy responses for MBC patients with liver metastasis.

In summary, our studies established metastatic-niche specific metabolic vulnerabilities as a novel target by uncovering the potential of FMD to improve Fulv response in ER^+ liver MBC. We envision that metabolism-based therapies in combination with standard endocrine-based therapies may be effective in exploiting metastatic site-specific metabolic dependencies of cancer cells, and in eliciting durable responses. Given the need for better strategies to treat liver metastatic tumors, our work offers both novel metabolic insights and a more complete understanding of the basic molecular mechanisms that underlie drug resistance. This novel understanding will enable us and others to exploit these new vulnerabilities to improve therapy response of MBCs, and reduce morbidity and mortality associated with liver metastasis.

Acknowledgements: Clinical data were provided from the Breast Cancer Management System database that is maintained and managed by the Department of Breast Medical Oncology from the University of Texas MD Anderson Cancer Center. We would like to thank members of UIUC Roy J. Carver Biotechnology Center. Specifically, Lucas Li and Alex Ulanov for metabolomics analysis and Alvaro Hernandez, Chris Wright and Kate Janssen for bulk and spatial sequencing analysis. This work was supported by grants from the University of Illinois, Office of the Vice Chancellor for Research, Future Interdisciplinary Research Endeavors grant from college of ACES, and National Institute of Food and Agriculture, U.S. Department of Agriculture, award ILLU-698-909 (to ZME). Research reported in this publication was supported by the Cancer Scholars for Translational and Applied Research (CSTAR)

Program sponsored by the Cancer Center at Illinois and the Carle Cancer Center under Award Number CST EP082021 (to ANM). The content is solely the responsibility of the authors and does not necessarily represent the official views of the program sponsors. Research reported in this publication was supported by the National Institute of Biomedical Imaging and Bioengineering of the National Institutes of Health under Award Number T32EB019944 (to ASC). The content is solely the responsibility of the authors and does not necessarily represent the official views of the National Institutes of Health. BHP is supported by the Susan G. Komen Foundation and the Breast Cancer Research Foundation. BSK was supported by a Breast Cancer Research grant 20-083.

References

1. Howlader, N., et al., *SEER cancer statistics review, 1975–2017*. National Cancer Institute, 2020.
2. Soni, A., et al., *Breast cancer subtypes predispose the site of distant metastases.* American journal of clinical pathology, 2015. **143**(4): p. 471-478.
3. Gupta, G.P. and J. Massagué, *Cancer metastasis: building a framework.* Cell, 2006. **127**(4): p. 679-695.
4. Mariotto, A.B., et al., *Estimation of the number of women living with metastatic breast cancer in the United States.* Cancer Epidemiology and Prevention Biomarkers, 2017. **26**(6): p. 809-815.
5. Eng, L.G., et al., *Ten-year survival in women with primary stage IV breast cancer.* Breast cancer research and treatment, 2016. **160**(1): p. 145-152.
6. Xie, Y., et al., *Treatment after Progression on Fulvestrant among Metastatic Breast Cancer Patients in Clinical Practice: a Multicenter, Retrospective Study.* Scientific Reports, 2019. **9**(1): p. 1710.
7. Koi, Y., et al., *Impact of Visceral Metastasis on Efficacy of Fulvestrant in Patients with Hormone Receptor-positive Recurrent Breast Cancer.* Anticancer Research, 2018. **38**(3): p. 1579-1584.
8. Regierer, A.C., et al., *An internally and externally validated prognostic score for metastatic breast cancer: analysis of 2269 patients.* Ann Oncol, 2014. **25**(3): p. 633-638.
9. Cummings, M.C., et al., *Metastatic progression of breast cancer: insights from 50 years of autopsies.* J Pathol, 2014. **232**(1): p. 23-31.
10. Cardoso, F., et al., *5th ESO-ESMO international consensus guidelines for advanced breast cancer (ABC 5).* Ann Oncol, 2020. **31**(12): p. 1623-1649.
11. Cardoso, F., et al., *4th ESO-ESMO International Consensus Guidelines for Advanced Breast Cancer (ABC 4)dagger.* Ann Oncol, 2018. **29**(8): p. 1634-1657.
12. Gong, Y., et al., *Impact of molecular subtypes on metastatic breast cancer patients: a SEER population-based study.* Scientific reports, 2017. **7**: p. 45411-45411.
13. Rugo, H.S., et al., *Endocrine Therapy for Hormone Receptor–Positive Metastatic Breast Cancer: American Society of Clinical Oncology Guideline.* Journal of Clinical Oncology, 2016. **34**(25): p. 3069-3103.
14. Palumbo, R., et al., *Patterns of treatment and outcome with 500-mg fulvestrant in postmenopausal women with hormone receptor-positive/HER2-negative metastatic breast cancer: a real-life multicenter Italian experience.* Therapeutic Advances in Medical Oncology, 2019. **11**: p. 1758835919833864.
15. Aksoy, C., *The X-Ray fluorescence parameters and radiation shielding efficiency of silver doped superconducting alloys.* Radiation Physics and Chemistry, 2021. **186**.
16. Bergers, G. and S.-M. Fendt, *The metabolism of cancer cells during metastasis.* Nature Reviews Cancer, 2021.

17. Pavlova, Natalya N. and Craig B. Thompson, *The Emerging Hallmarks of Cancer Metabolism.* Cell Metabolism, 2016. **23**(1): p. 27-47.
18. Hanahan, D. and Robert A. Weinberg, *Hallmarks of Cancer: The Next Generation.* Cell, 2011. **144**(5): p. 646-674.
19. Cotul, E.K., et al., *Combined Targeting of Estrogen Receptor Alpha and Exportin 1 in Metastatic Breast Cancers.* Cancers (Basel), 2020. **12**(9).
20. Andrzejewski, S., et al., *PGC-1α Promotes Breast Cancer Metastasis and Confers Bioenergetic Flexibility against Metabolic Drugs.* Cell Metabolism, 2017. **26**(5): p. 778-787.e5.
21. LeBleu, V.S., et al., *PGC-1α mediates mitochondrial biogenesis and oxidative phosphorylation in cancer cells to promote metastasis.* Nature cell biology, 2014. **16**(10): p. 992-15.
22. Laws, M.J., et al., *Suppression of breast cancer metastasis and extension of survival by a new antiestrogen in a preclinical model driven by mutant estrogen receptors.* Breast Cancer Research and Treatment, 2020. **181**(2): p. 297-307.
23. Laws, M.J., et al., *Suppression of breast cancer metastasis and extension of survival by a new antiestrogen in a preclinical model driven by mutant estrogen receptors.* Breast Cancer Res Treat, 2020. **181**(2): p. 297-307.
24. Wrobel, K., et al., *ERα-XPO1 crosstalk controls tamoxifen sensitivity in tumors by altering ERK5 cellular localization.* Molecular Endocrinology, 2016. **0**(0): p. me.2016-1101.
25. Alexander, T.B., et al., *Phase I Study of Selinexor, a Selective Inhibitor of Nuclear Export, in Combination With Fludarabine and Cytarabine, in Pediatric Relapsed or Refractory Acute Leukemia.* J Clin Oncol, 2016. **34**(34): p. 4094-4101.
26. Gounder, M.M., et al., *Phase IB Study of Selinexor, a First-in-Class Inhibitor of Nuclear Export, in Patients With Advanced Refractory Bone or Soft Tissue Sarcoma.* J Clin Oncol, 2016. **34**(26): p. 3166-74.
27. Abdul Razak, A.R., et al., *First-in-Class, First-in-Human Phase I Study of Selinexor, a Selective Inhibitor of Nuclear Export, in Patients With Advanced Solid Tumors.* J Clin Oncol, 2016. **34**(34): p. 4142-4150.
28. Bolger, A.M., M. Lohse, and B. Usadel, *Trimmomatic: a flexible trimmer for Illumina sequence data.* Bioinformatics, 2014. **30**(15): p. 2114-20.
29. Zerbino, D.R., et al., *Ensembl 2018.* Nucleic Acids Res, 2018. **46**(D1): p. D754-D761.
30. Dobin, A., et al., *STAR: ultrafast universal RNA-seq aligner.* Bioinformatics, 2013. **29**(1): p. 15-21.
31. Liao, Y., G.K. Smyth, and W. Shi, *The Subread aligner: fast, accurate and scalable read mapping by seed-and-vote.* Nucleic Acids Res, 2013. **41**(10): p. e108.
32. Robinson, M.D., D.J. McCarthy, and G.K. Smyth, *edgeR: a Bioconductor package for differential expression analysis of digital gene expression data.* Bioinformatics, 2010. **26**(1): p. 139-40.
33. Ritchie, M.E., et al., *limma powers differential expression analyses for RNA-sequencing and microarray studies.* Nucleic Acids Res, 2015. **43**(7): p. e47.
34. Phipson, B., et al., *Robust Hyperparameter Estimation Protects against Hypervariable Genes and Improves Power to Detect Differential Expression.* Ann Appl Stat, 2016. **10**(2): p. 946-963.
35. de Hoon, M.J., et al., *Open source clustering software.* Bioinformatics, 2004. **20**(9): p. 1453-4.
36. Rhodes, D.R., et al., *ONCOMINE: a cancer microarray database and integrated data-mining platform.* Neoplasia, 2004. **6**(1): p. 1-6.
37. Chong, J., D.S. Wishart, and J. Xia, *Using MetaboAnalyst 4.0 for comprehensive and integrative metabolomics data analysis.* Current protocols in bioinformatics, 2019. **68**(1): p. e86.
38. Madak-Erdogan, Z., et al., *Design of pathway preferential estrogens that provide beneficial metabolic and vascular effects without stimulating reproductive tissues.* Science signaling, 2016. **9**(429): p. ra53-ra53.
39. Madak-Erdogan, Z., et al., *Novel roles for ERK5 and cofilin as critical mediators linking ERα-driven transcription, actin reorganization, and invasiveness in breast cancer.* Molecular Cancer Research, 2014. **12**(5): p. 714-727.
40. Madak-Erdogan, Z., et al., *Free fatty acids rewire cancer metabolism in obesity-associated breast cancer via estrogen receptor and mTOR signaling.* Cancer Research, 2019: p. canres.2849.2018.
41. Zhao, Y.C. and Z. Madak Erdogan, *Systems Biology of Metabolic Regulation by Estrogen Receptor Signaling in Breast Cancer.* J Vis Exp, 2016(109).
42. Chandarlapaty, S., et al., *Prevalence of esr1 mutations in cell-free dna and outcomes in metastatic breast cancer: A secondary analysis of the bolero-2 clinical trial.* JAMA Oncology, 2016. **2**(10): p. 1310-1315.
43. Clatot, F., et al., *Kinetics, prognostic and predictive values of ESR1 circulating mutations in metastatic breast cancer patients progressing on aromatase inhibitor.* Oncotarget, 2016. **7**(46): p. 74448-74459.

44. Fribbens, C., et al., *Plasma ESR1 Mutations and the Treatment of Estrogen Receptor–Positive Advanced Breast Cancer*. Journal of Clinical Oncology, 2016. **34**(25): p. 2961-2968.
45. Schiavon, G., et al., *Analysis of ESR1 mutation in circulating tumor DNA demonstrates evolution during therapy for metastatic breast cancer*. Science Translational Medicine, 2015. **7**(313): p. 313ra182-313ra182.
46. Rinaldi, J., et al., *The genomic landscape of metastatic breast cancer: Insights from 11,000 tumors.* PLOS ONE, 2020. **15**(5): p. e0231999.
47. Desmedt, C., et al., *ESR1 mutations in metastatic lobular breast cancer patients*. npj Breast Cancer, 2019. **5**(1): p. 9.
48. Reinert, T., et al., *Association of ESR1 Mutations and Visceral Metastasis in Patients with Estrogen Receptor-Positive Advanced Breast Cancer from Brazil.* Journal of Oncology, 2019. **2019**: p. 1947215.
49. Caffa, I., et al., *Fasting-mimicking diet and hormone therapy induce breast cancer regression.* Nature, 2020. **583**(7817): p. 620-624.
50. Jin, M.-Z. and W.-L. Jin, *The updated landscape of tumor microenvironment and drug repurposing.* Signal Transduction and Targeted Therapy, 2020. **5**(1): p. 166.
51. Dees, E.C. and L.A. Carey, *Improving endocrine therapy for breast cancer: it's not that simple.* J Clin Oncol, 2013. **31**(2): p. 171-3.
52. Guenthart, B.A., et al., *Regeneration of severely damaged lungs using an interventional cross-circulation platform.* Nature communications, 2019. **10**(1): p. 1985-1985.
53. Dorrello, N.V., et al., *Functional vascularized lung grafts for lung bioengineering.* Science advances, 2017. **3**(8): p. e1700521-e1700521.
54. Wells, R.G., *The role of matrix stiffness in regulating cell behavior.* Hepatology, 2008. **47**(4): p. 1394-1400.
55. Miedel, M.T., et al., *Modeling the Effect of the Metastatic Microenvironment on Phenotypes Conferred by Estrogen Receptor Mutations Using a Human Liver Microphysiological System.* Scientific reports, 2019. **9**(1): p. 8341-8341.
56. Achinger-Kawecka, J., et al., *Epigenetic reprogramming at estrogen-receptor binding sites alters 3D chromatin landscape in endocrine-resistant breast cancer*. Nature Communications, 2020. **11**(1): p. 320.
57. Murakami, S., A. Nagari, and W.L. Kraus, *Dynamic assembly and activation of estrogen receptor α enhancers through coregulator switching.* Genes & development, 2017. **31**(15): p. 1535-1548.
58. Fu, X., et al., *FOXA1 upregulation promotes enhancer and transcriptional reprogramming in endocrine-resistant breast cancer*. Proceedings of the National Academy of Sciences, 2019. **116**(52): p. 26823-26834.
59. Magnani, L., et al., *Genome-wide reprogramming of the chromatin landscape underlies endocrine therapy resistance in breast cancer*. Proceedings of the National Academy of Sciences, 2013. **110**(16): p. E1490-E1499.
60. Jeselsohn, R., et al., *Allele-Specific Chromatin Recruitment and Therapeutic Vulnerabilities of ESR1 Activating Mutations.* Cancer Cell, 2018. **33**(2): p. 173-186.e5.
61. McDonald, O.G., et al., *Epigenomic reprogramming during pancreatic cancer progression links anabolic glucose metabolism to distant metastasis.* Nature genetics, 2017. **49**(3): p. 367-376.
62. Makohon-Moore, A.P., et al., *Limited heterogeneity of known driver gene mutations among the metastases of individual patients with pancreatic cancer*. Nature Genetics, 2017. **49**(3): p. 358-366.
63. Faubert, B., A. Solmonson, and R.J. DeBerardinis, *Metabolic reprogramming and cancer progression.* Science, 2020. **368**(6487): p. eaaw5473.
64. Pascual, G., D. Domínguez, and S.A. Benitah, *The contributions of cancer cell metabolism to metastasis.* Disease models & mechanisms, 2018. **11**(8): p. dmm032920.
65. Boukouris, A.E., S.D. Zervopoulos, and E.D. Michelakis, *Metabolic Enzymes Moonlighting in the Nucleus: Metabolic Regulation of Gene Transcription.* Trends in Biochemical Sciences, 2016. **41**(8): p. 712-730.
66. Sutendra, G., et al., *A Nuclear Pyruvate Dehydrogenase Complex Is Important for the Generation of Acetyl-CoA and Histone Acetylation.* Cell, 2014. **158**(1): p. 84-97.
67. Matsuda, S., et al., *Nuclear pyruvate kinase M2 complex serves as a transcriptional coactivator of arylhydrocarbon receptor*. Nucleic Acids Research, 2016. **44**(2): p. 636-647.
68. Li, X., et al., *Nucleus-Translocated ACSS2 Promotes Gene Transcription for Lysosomal Biogenesis and Autophagy*. Molecular cell, 2017. **66**(5): p. 684-697.e9.
69. Li, X., X. Qian, and Z. Lu, *Local histone acetylation by ACSS2 promotes gene transcription for lysosomal biogenesis and autophagy*. Autophagy, 2017. **13**(10): p. 1790-1791.

70. Wellen, K.E., et al., *ATP-citrate lyase links cellular metabolism to histone acetylation.* Science, 2009. **324**(5930): p. 1076-80.
71. Levesque, S., et al., *Trial watch: dietary interventions for cancer therapy*. Oncoimmunology, 2019. **8**(7): p. 1591878.
72. Masood, W., P. Annamaraju, and K.R. Uppaluri, *Ketogenic diet.* StatPearls [Internet], 2020.
73. Puchalska, P. and P.A. Crawford, *Multi-dimensional Roles of Ketone Bodies in Fuel Metabolism, Signaling, and Therapeutics.* Cell Metabolism, 2017. **25**(2): p. 262-284.
74. Poff, A.M., et al., *The ketogenic diet and hyperbaric oxygen therapy work synergistically to slow tumor growth and increase survival time in mice with systemic metastatic cancer*. Faseb Journal, 2013. **27**.
75. Otto, C., et al., *Growth of human gastric cancer cells in nude mice is delayed by a ketogenic diet supplemented with omega-3 fatty acids and medium-chain triglycerides.* Bmc Cancer, 2008. **8**.
76. Allen, B.G., et al., *Ketogenic diets as an adjuvant cancer therapy: History and potential mechanism.* Redox Biology, 2014. **2**: p. 963-970.
77. Hopkins, B.D., et al., *Suppression of insulin feedback enhances the efficacy of PI3K inhibitors.* Nature, 2018. **560**(7719): p. 499-503.

Figure legends

Figure 1: Patients with liver metastatic breast tumors experience poor response to Fulv. MD Anderson Cancer Center cohort study involved 1832 patients without liver MBC and 1556 with liver MBC. Number of dead and alive patients with and without liver MBC were compared using Fisher's exact test **A, B)** Patients with ER^{+}/$HER2^{-}$ liver metastatic tumors have shorter overall survival when treated with Fulv therapies, both monotherapy and combined treatment with CDK4/6 inhibitor, PI3K inhibitor, or mTOR inhibitor. Log-rank test was used to compare survival curves. **C)** Colony formation assay for MCF7-*ESR1*^{Y537S} cells in Matrigel or decellularized hydrogels from different metastatic tissues and **D)** and efficacy of 1 μM Fulv to reduce colony number. Colonies were treated for 3 weeks. Unpaired t-test, P-values are indicated.

Figure 2: ER^{+} MBC cells display distinct transcriptomes and ER cistromes when grown in different hydrogels. A) Hierarchical clustering of RNASeq data of MCF7-ESR1^{Y537S} cells grown on 2D (plastic), bone, liver, or lung Native Coat ECMs for 24 hours. Total RNA was isolated, and sequencing was performed using three samples

from each treatment group. Differentially expressed genes were determined with P <0.05 and expression fold change >2. **B)** Principal component analysis of gene expression data using differentially expressed genes list from **A**, which shows distinct gene expression profiles associated with different hydrogels. **C)** Gene-set enrichment analysis of gene sets that were enriched in related genes as classical targets of ERα action dataset. **D)** ERα protein expression was examined using western blotting. B-actin was used as a loading control. **E)** ERα ChIP-Seq in MCF7-ESR1^{Y537S} cells grown on plastic (2D), bone, liver, or lung hydrogels. ERα–DNA complexes were pulled down using ERα antibodies. Three biological replicates were pooled and sequenced. Clustering of ERα-binding sites in hydrogels was done using seqMINER software. The ERα-binding sites were separated into four clusters of characteristic patterns: C1, C2, C3, and C4. **F)** Example histogram showing ERα recruitment to GREB1 binding sites in cells grown in different hydrogels. **G)** Feature distribution of binding sites.

Figure 3: Glucose dependency is increased in MCF7-ESR1^{Y537S} cells cultured in liver hydrogels with Fulv treatment. A) Cell metabolic phenotype assay using the Seahorse Cell Energy Phenotype Kit. Cells cultured in plates coated with bone, liver, and lung hydrogels for 24 hours were tested for the energy phenotype. Each experiment was replicated twice with three technical replicates. Results from a representative experiment are shown. **B)** Whole metabolite profiling using GC/MS analysis of extracts from MCF7-ESR1^{Y537S} grown on plastic (Ctrl), bone, lung, and liver hydrogels. Scores plot showing distinct metabolite abundance patterns on different hydrogels. **C)** Heatmap of metabolite profiling analysis of pathway changes induced by different hydrogels. **D)** Cell phenotype assays were performed to dissect the specific fuel dependency on

different hydrogels, which showed that liver hydrogels but not bone or lung hydrogels increased glycolytic respiration in the presence of full media, or media with glucose or pyruvate compared to cells that were grown on plastic. Two-way ANOVA, Dunn's test, *p<0.05. **E)** Liver ECM led to an increase in oxidative respiration only when cells were supplemented with full media. **F)** Cell metabolic phenotype assay showed that MBC cells grown on liver ECM in media with glucose increased in glycolytic potential. **G)** Whole-metabolite profiling in MBC cells grown on plates coated with liver ECM and treated with vehicle (Veh) or 1 µM Fulv for 24 hours.

Figure 4: ER^+ Liver metastatic xenograft tumors do not respond to Fulv. A) MCF7-$ESR1^{Y537S}$ cells were grafted intravenously (tail vein), and mice were treated with placebo or Fulv. Metastatic burden was measured using IVIS to detect bioluminescence. N=6, metastatic tumor luciferase signal from each mouse is plotted. No statistically significant difference was detected in metastatic burden with Fulv using a two-way ANOVA for Fulv effect over time. **B)** Imaging of luciferase signal indicating metastatic outgrowth in the livers, lungs, and bones**. C)** RNA was isolated from the liver tumors. mRNA expression of ERα target genes GREB1 and PgR, and cell cycle-related genes PCNA and Ki67 were measured by qRT-PCR. Unpaired t-test, p values are indicated. **D)** Spatial scSeq of 2 Veh and 2 Fulv tumors. UMAP plots **E)** 22 clusters were identified **F)** Level of human transcripts identified in xenograft tumors **G)** Spatial expression of genes of interest.

Figure 5: Metastatic burden increases with increasing carbohydrate percentage in the diet. **A)** RNA was isolated from the liver metastatic tumors of MCF7-$ESR1^{Y537S}$ xenografts and RNASeq was performed using 6 samples from each treatment group.

Fulv significantly increased glycolysis and glycogenesis metabolism pathways, as well as lipid metabolism. Pink-labeled genes are upregulated, and blue-labeled genes are downregulated. **B)** Comparison of glycolysis, glycogenesis, and lipid metabolism-related genes in the MCF7-ESR1^{Y537S} liver tumors, mouse transcripts identified in these tumors, in MCF7-ESR1^{Y537S} cells grown plastic re treated with Veh or 1μM Fulv, Palb or 4OHT, and MCF7-*ESR1*^{Y537S} cells grown on plates coated with different hydrogels. Fold change relative to Veh-treated samples is plotted in each dataset. **C)** NGS mice with MCF7-ESR1^{Y537S} xenografts were fed a control diet, HFD, or FMD. Metastatic burden was measured using IVIS to detect bioluminescence. **D)** Mean Luminescence intensity of tumors was plotted to determine metastatic burden. N=3, Two-way ANOVA, Tukey's post hoc test, * p <0.05, ***p <0.001, **** p <0.0001. Bars represent SEM. **E)** Livers from corresponding animals in A. **F)** Pearson correlations and p-values showing correlation between metastatic burden and carbohydrate content of the diets. **G)** Histological analysis of tumors from (A). HE, ERα, PAS, and PAS-D IHC staining were performed.

Figure 6: FMD diet synergizes with Fulv to reduce MCF7-ESR1^{Y537S} liver metastatic burden and number of nodules. A, B) NGS mice with MCF7-ESR1^{Y537S} xenografts were fed control diet or FMD. Mice were treated with Veh or Fulv. Bioluminescence imaging of tumors was measured by IVIS. **C)** Representative images of livers from mice in different treatment groups. **D)** Liver metastatic nodules were counted at necropsy. One-way ANOVA, Dunn's multiple comparison test, *p<0.05. **E)** Histological analysis of tumors from (A). HE, ERα, PAS, and PAS-D IHC staining were performed.

A

Groups	Median overall survival, years (95% CI)	HR (95% CI)	P-value
Non-liver Metastasis	13.1 (12.5, 13.9)	Reference	
Liver Metastasis	10.0 (9.6, 10.4)	1.46 (1.34, 1.59)	<0.001

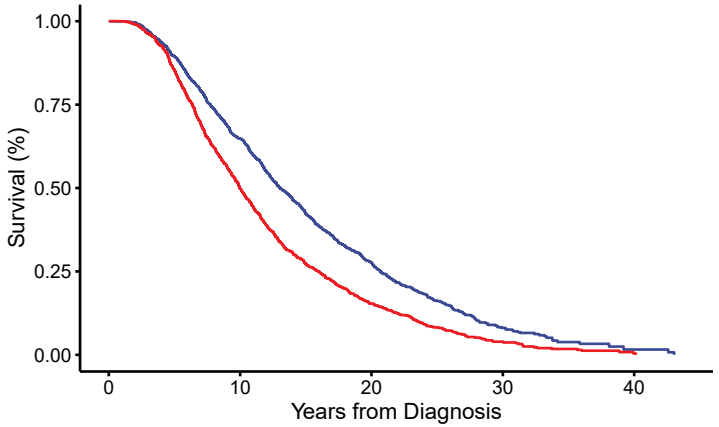

B

Groups	Median survival, years (95% CI)	HR (95% CI)	P-value
Non-liver Metastasis	6.7 (6.5, 7)	Reference	
Liver Metastasis	5.8 (5.6, 6)	1.3 (1.2, 1.5)	<0.001*

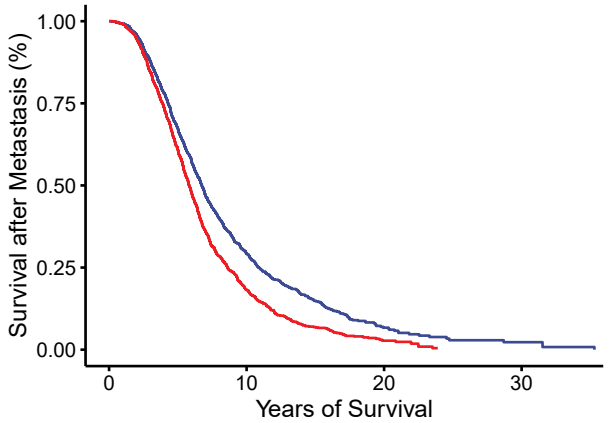

C

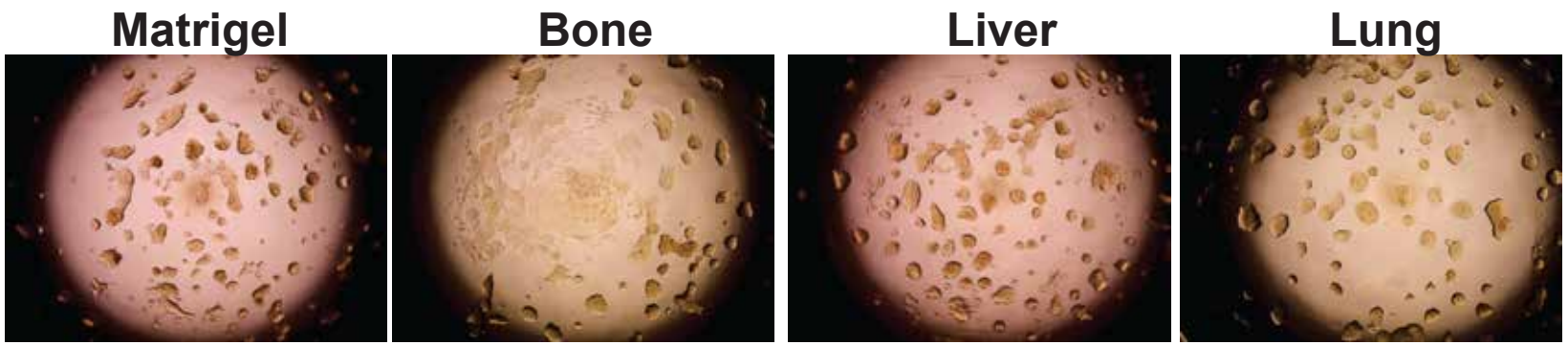

D

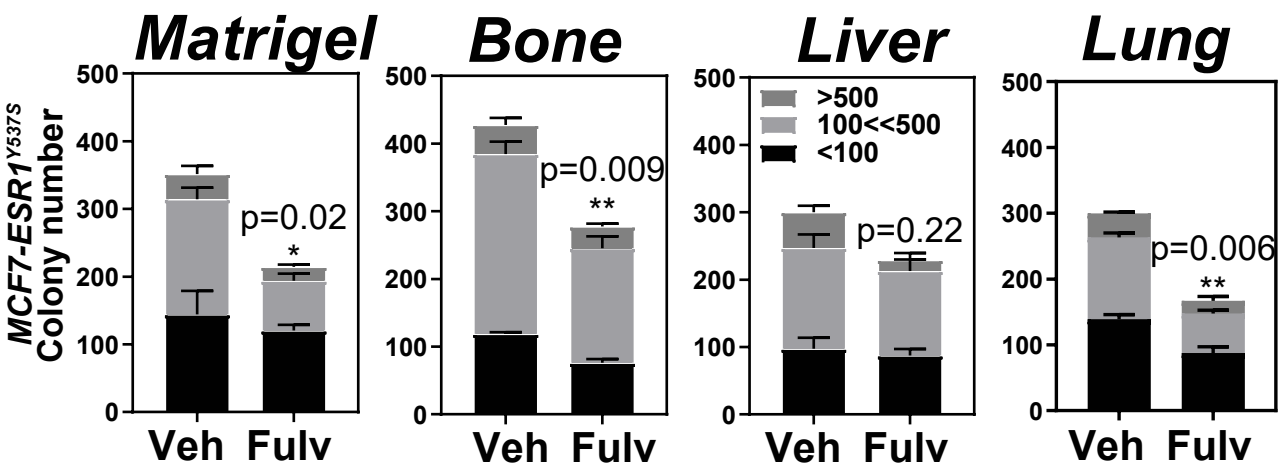

Figure 1

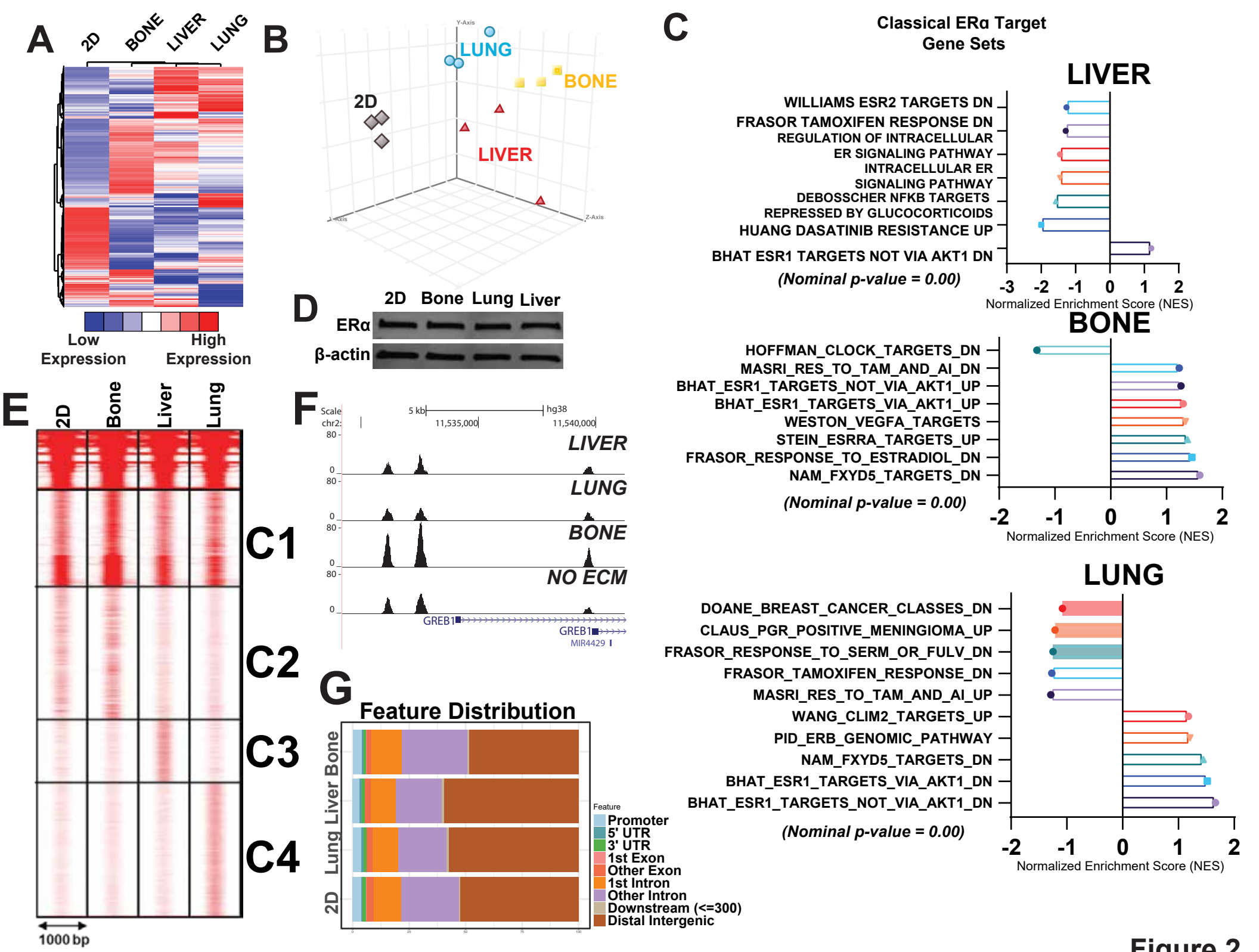
A
2D
BONE
LIVER
LUNG
Low Expression
High Expression
B
LUNG
BONE
2D
LIVER
C
Classical ERα Target Gene Sets
LIVER
WILLIAMS ESR2 TARGETS DN
FRASOR TAMOXIFEN RESPONSE DN
REGULATION OF INTRACELLULAR
ER SIGNALING PATHWAY
INTRACELLULAR ER
SIGNALING PATHWAY
DEBOSSCHER NFKB TARGETS
REPRESSED BY GLUCOCORTICOIDS
HUANG DASATINIB RESISTANCE UP
BHAT ESR1 TARGETS NOT VIA AKT1 DN
(Nominal p-value = 0.00)
-3 -2 -1 0 1 2
Normalized Enrichment Score (NES)
BONE
HOFFMAN_CLOCK_TARGETS_DN
MASRI_RES_TO_TAM_AND_AI_DN
BHAT_ESR1_TARGETS_NOT_VIA_AKT1_UP
BHAT_ESR1_TARGETS_VIA_AKT1_UP
WESTON_VEGFA_TARGETS
STEIN_ESRRA_TARGETS_UP
FRASOR_RESPONSE_TO_ESTRADIOL_DN
NAM_FXYD5_TARGETS_DN
(Nominal p-value = 0.00)
-2 -1 0 1 2
Normalized Enrichment Score (NES)
LUNG
DOANE_BREAST_CANCER_CLASSES_DN
CLAUS_PGR_POSITIVE_MENINGIOMA_UP
FRASOR_RESPONSE_TO_SERM_OR_FULV_DN
FRASOR_TAMOXIFEN_RESPONSE_DN
MASRI_RES_TO_TAM_AND_AI_UP
WANG_CLIM2_TARGETS_UP
PID_ERB_GENOMIC_PATHWAY
NAM_FXYD5_TARGETS_DN
BHAT_ESR1_TARGETS_VIA_AKT1_DN
BHAT_ESR1_TARGETS_NOT_VIA_AKT1_DN
(Nominal p-value = 0.00)
-2 -1 0 1 2
Normalized Enrichment Score (NES)
D
2D Bone Lung Liver
ERα
β-actin
E
2D
Bone
Liver
Lung
C1
C2
C3
C4
1000 bp
F
Scale
5 kb
hg38
chr2:
11,535,000
11,540,000
LIVER
LUNG
BONE
NO ECM
GREB1
GREB1
MIR4429
G
Feature Distribution
2D Lung Liver Bone
Feature
Promoter
5' UTR
3' UTR
1st Exon
Other Exon
1st Intron
Other Intron
Downstream (<=300)
Distal Intergenic

Figure 2

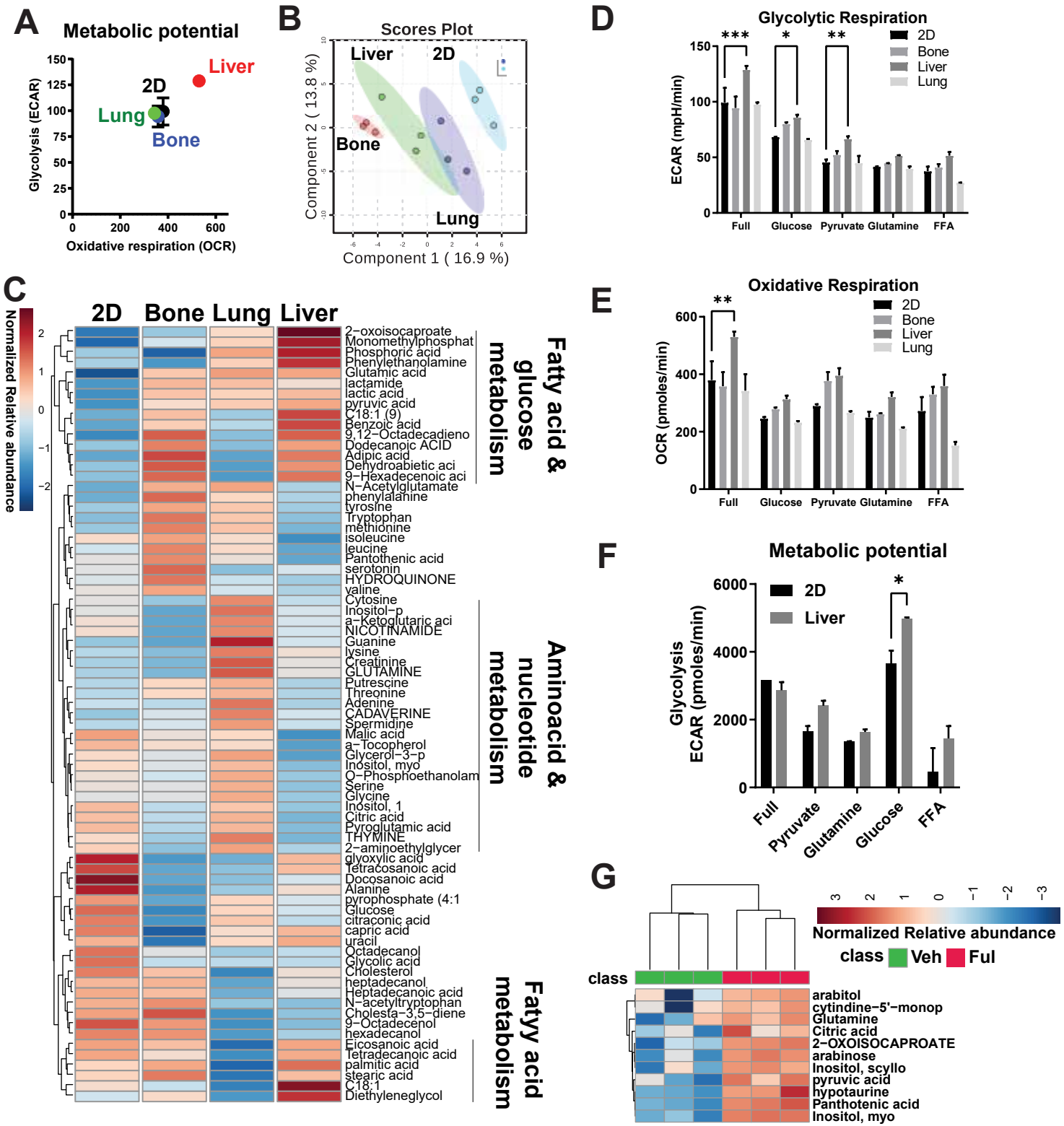
A
Metabolic potential
Glycolysis (ECAR)
Oxidative respiration (OCR)
Liver
2D
Lung
Bone
B
Scores Plot
Component 2 (13.8 %)
Component 1 (16.9 %)
C
2D Bone Lung Liver
Normalized Relative abundance
Fatty acid & glucose metabolism
Aminoacid & nucleotide metabolism
Fatyy acid metabolism
2−oxoisocaproate
Monomethylphosphat
Phosphoric acid
Phenylethanolamine
Glutamic acid
lactamide
lactic acid
pyruvic acid
C18:1 (9)
Benzoic acid
9,12−Octadecadieno
Dodecanoic ACID
Adipic acid
Dehydroabietic aci
9−Hexadecenoic aci
N−Acetylglutamate
phenylalanine
tyrosine
Tryptophan
methionine
isoleucine
leucine
Pantothenic acid
serotonin
HYDROQUINONE
valine
Cytosine
Inositol−p
a−Ketoglutaric aci
NICOTINAMIDE
Guanine
lysine
Creatinine
GLUTAMINE
Putrescine
Threonine
Adenine
CADAVERINE
Spermidine
Malic acid
a−Tocopherol
Glycerol−3−p
Inositol, myo
O−Phosphoethanolam
Serine
Glycine
Inositol, 1
Citric acid
Pyroglutamic acid
THYMINE
2−aminoethylglycer
glyoxylic acid
Tetracosanoic acid
Docosanoic acid
Alanine
pyrophosphate (4:1
Glucose
citraconic acid
capric acid
uracil
Octadecanol
Glycolic acid
Cholesterol
heptadecanol
Heptadecanoic acid
N−acetyltryptophan
Cholesta−3,5−diene
9−Octadecenol
hexadecanol
Eicosanoic acid
Tetradecanoic acid
palmitic acid
stearic acid
C18:1
Diethyleneglycol
D
Glycolytic Respiration
ECAR (mpH/min)
2D
Bone
Liver
Lung
Full
Glucose
Pyruvate
Glutamine
FFA
E
Oxidative Respiration
OCR (pmoles/min)
F
Metabolic potential
Glycolysis ECAR (pmoles/min)
G
class
Normalized Relative abundance
class Veh Ful
arabitol
cytindine−5'−monop
Glutamine
Citric acid
2−OXOISOCAPROATE
arabinose
Inositol, scyllo
pyruvic acid
hypotaurine
Panthotenic acid
Inositol, myo

Figure 3

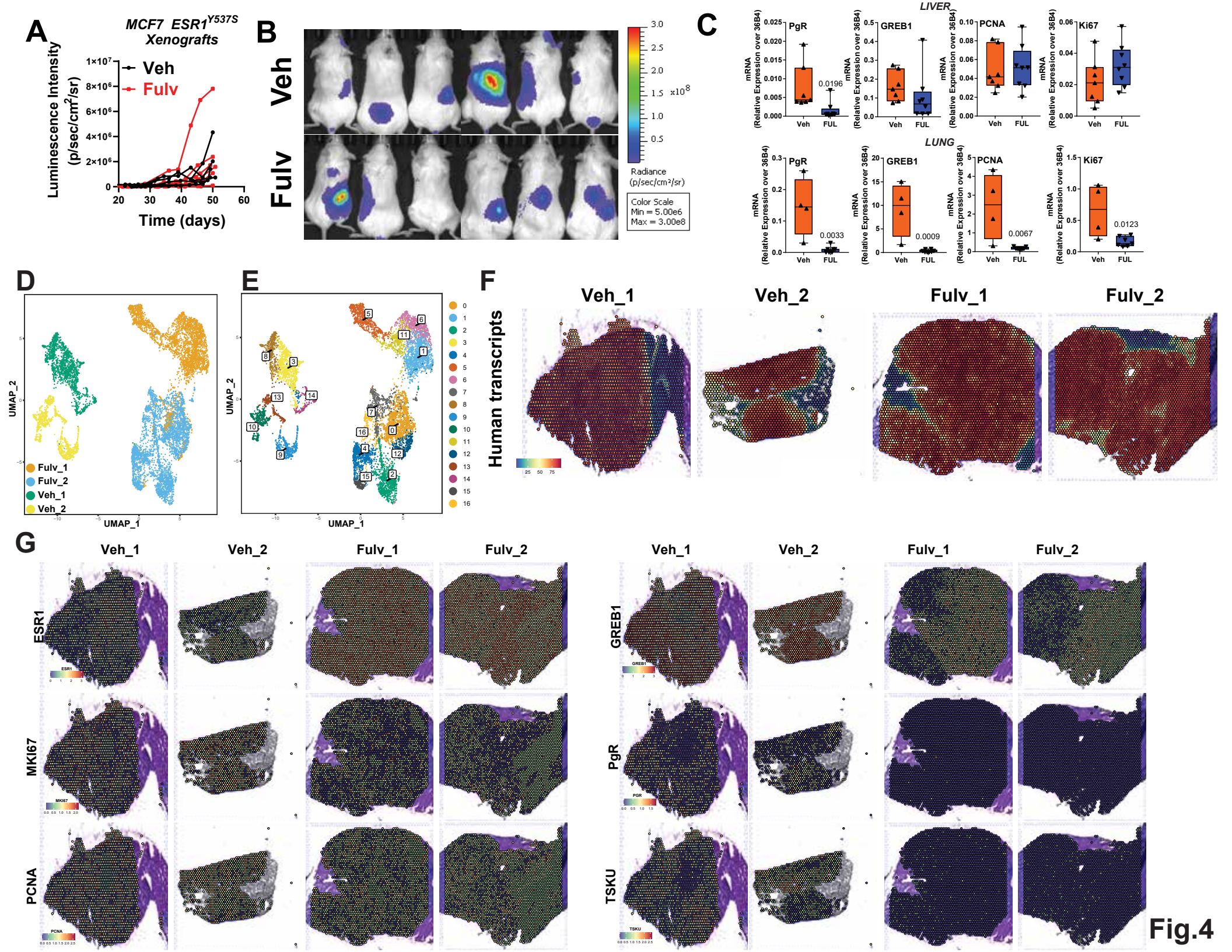
A
MCF7 ESR1Y537S Xenografts
Veh
Fulv
Luminescence Intensity (p/sec/cm²/sr)
Time (days)
B
Veh
Fulv
Radiance (p/sec/cm²/sr)
Color Scale Min = 5.00e6 Max = 3.00e8
C
LIVER
LUNG
PgR
GREB1
PCNA
Ki67
mRNA (Relative Expression over 36B4)
Veh
FUL
0.0196
0.0033
0.0009
0.0067
0.0123
D
UMAP_1
UMAP_2
Fulv_1
Fulv_2
Veh_1
Veh_2
E
F
Veh_1
Veh_2
Fulv_1
Fulv_2
Human transcripts
G
ESR1
MKI67
PCNA
GREB1
PgR
TSKU

Fig.4

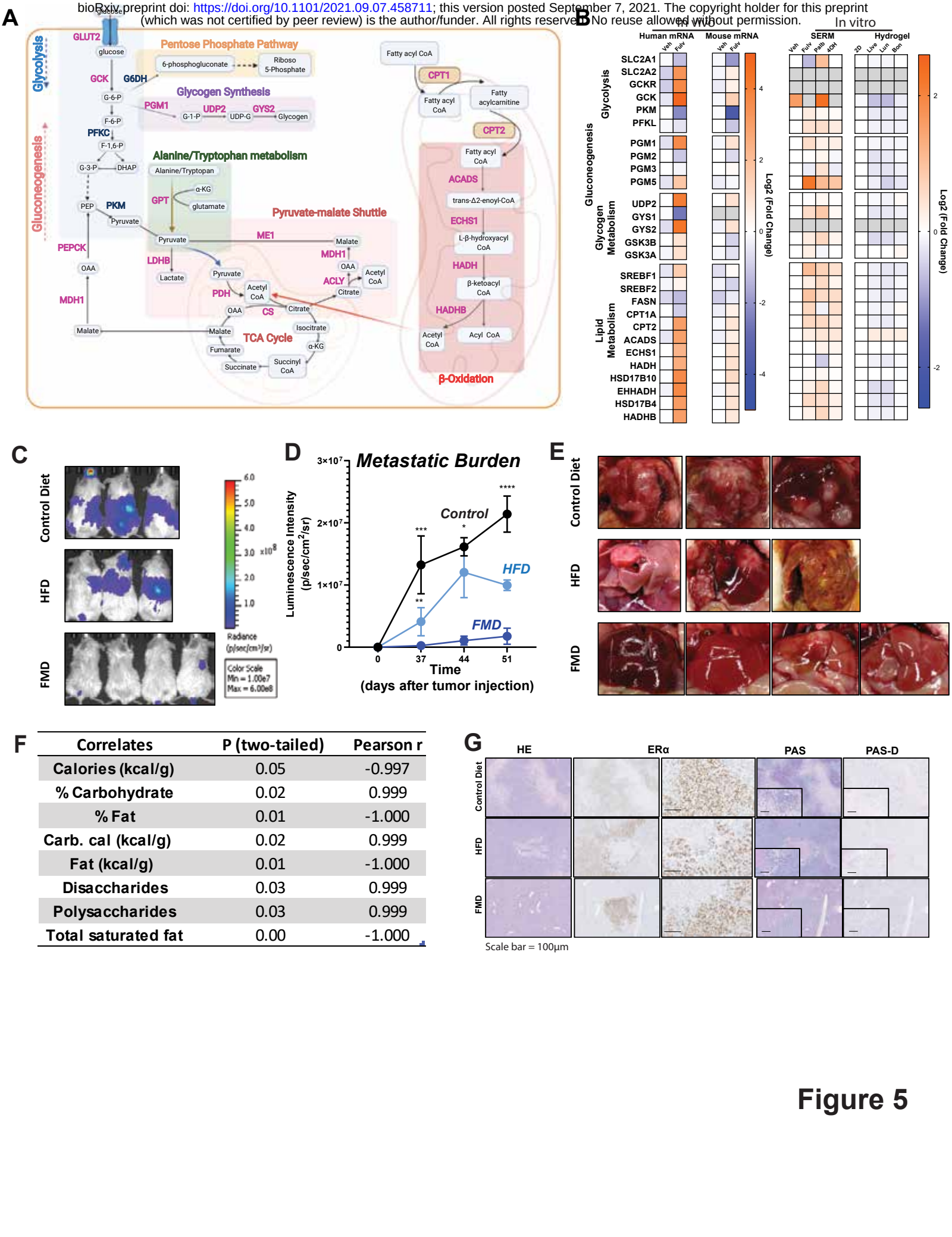

Correlates	P (two-tailed)	Pearson r
Calories (kcal/g)	0.05	-0.997
% Carbohydrate	0.02	0.999
% Fat	0.01	-1.000
Carb. cal (kcal/g)	0.02	0.999
Fat (kcal/g)	0.01	-1.000
Disaccharides	0.03	0.999
Polysaccharides	0.03	0.999
Total saturated fat	0.00	-1.000

Figure 5

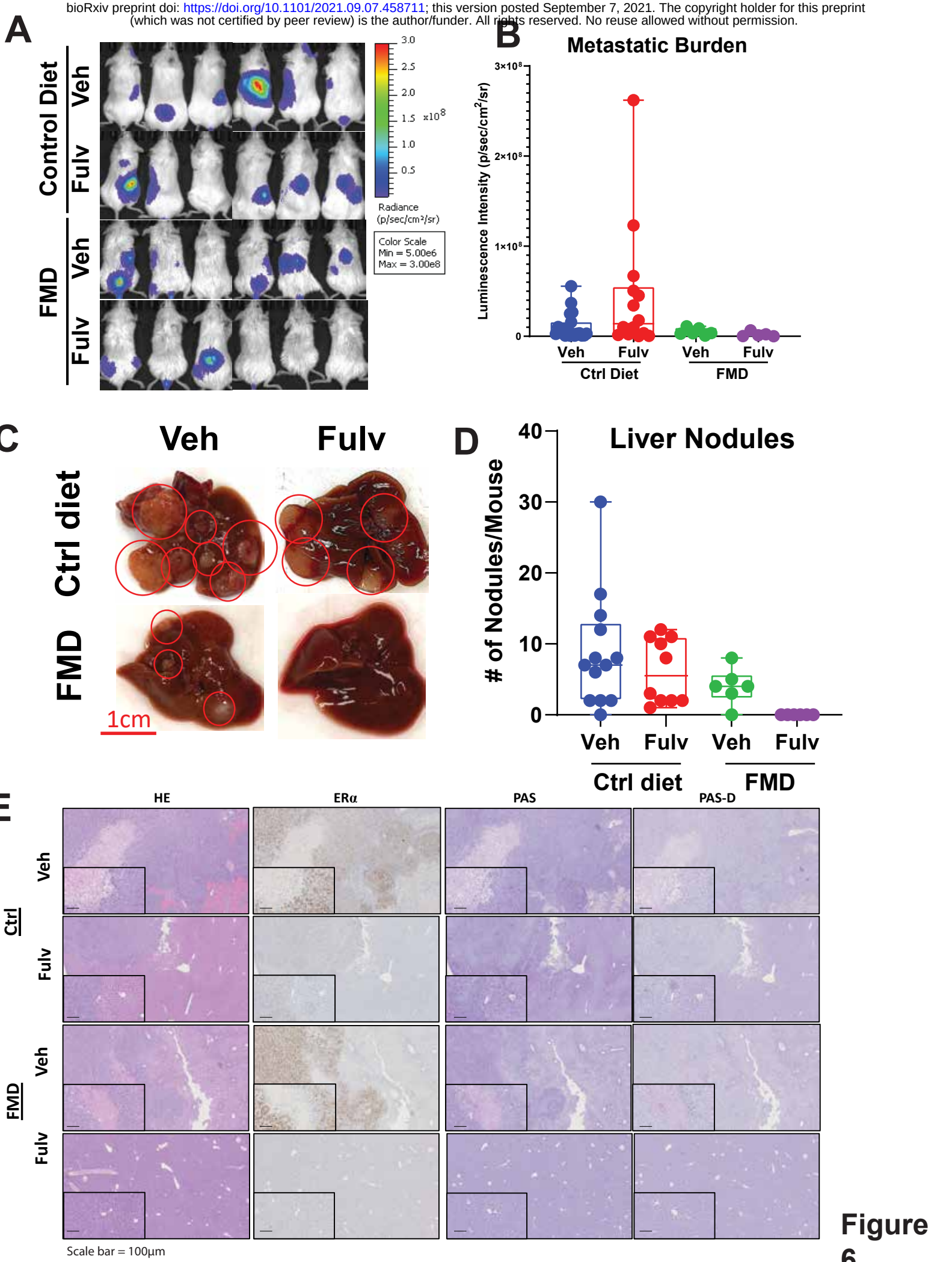

Figure 6

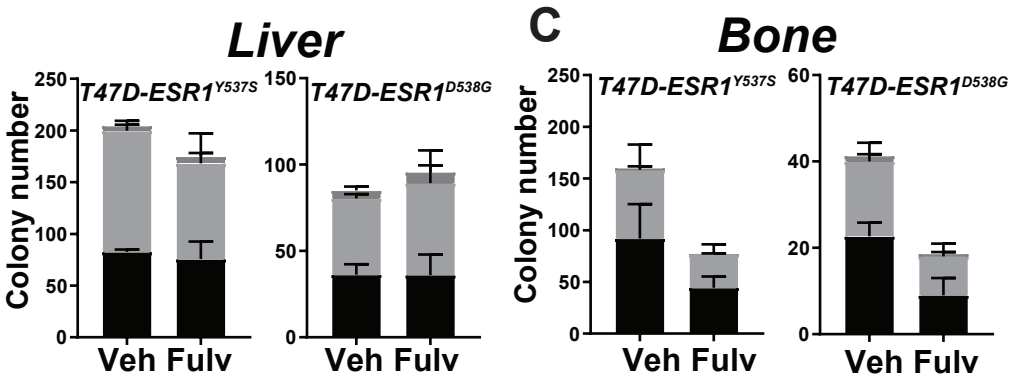

Supplementary Figure 1

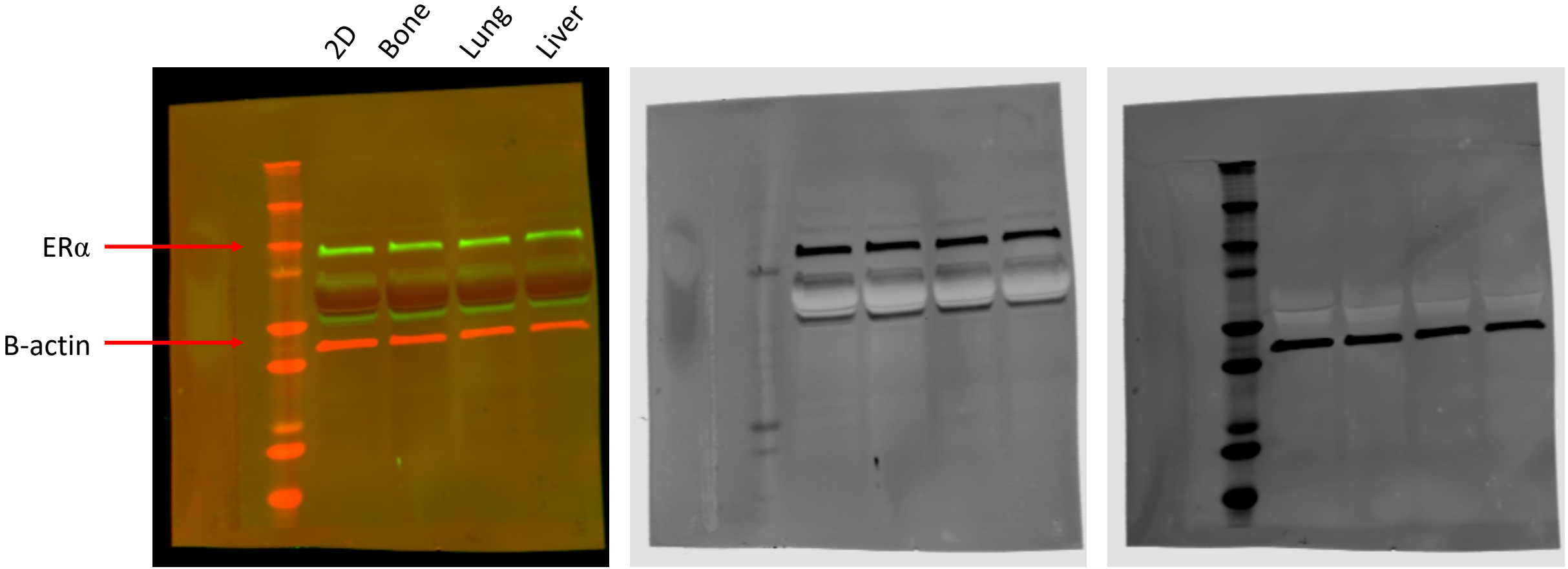

Supplementary Figure 2

	Control Diet	High Fat Diet	Fasting Mimicking Diet
Calories (kcal/gr)	3.93 kcal/gr	5.51 kcal/gr	7.24 kcal/gr
% Carbohydrate	61.6	36.2	3.2
%Fat	7.2	36	75.1
%Protein	20.5	20.5	8.6

Supplementary Table 1

	P (two-tailed)	Pearson r	R squared	P value summary
Calories(kcal/r)	0.0492	-0.997	0.994	*
Caloric Intake (kcal/Body weight)	0.946	-0.08474	0.007181	ns
Body weight	0.213	0.9445	0.8922	ns
% Carbohydrate	0.0244	0.9993	0.9985	*
% Fat	0.0103	-0.9999	0.9997	*
% Protein	0.2675	0.913	0.8336	ns
Carb. cal (kcal/g)	0.0233	0.9993	0.9987	*
Fat (kcal/g)	0.0108	-0.9999	0.9997	*
Prot. (kcal/g)	0.2675	0.913	0.8336	ns
Monosaccharides	0.2039	-0.9492	0.9009	ns
Disaccharides	0.0253	0.9992	0.9984	*
Polysaccharides	0.0339	0.9986	0.9972	*
18:2 Linoleic acid	0.097	-0.9884	0.9769	ns
18:3 Linoleic acid	0.0536	-0.9965	0.9929	ns
Total saturated fat	0.0022	-1	1	**
Total monounsaturated fat	0.0716	-0.9937	0.9874	ns
Total polyunsaturated fat	0.0899	-0.99	0.9802	ns
Ala	0.2675	0.913	0.8336	ns
Arg	0.2675	0.913	0.8336	ns
Asp	0.2675	0.913	0.8336	ns
Cys	0.2675	0.913	0.8336	ns
Glutamate	0.2675	0.913	0.8336	ns
Glycine	0.2675	0.913	0.8336	ns
Hist	0.2675	0.913	0.8336	ns
Iso	0.2675	0.913	0.8336	ns
Leu	0.2675	0.913	0.8336	ns
Lys	0.2675	0.913	0.8336	ns
Methionine	0.2675	0.913	0.8336	ns
Phen	0.2675	0.913	0.8336	ns
Prot cal	0.2675	0.913	0.8336	ns
Ser	0.2675	0.913	0.8336	ns
Thr	0.2675	0.913	0.8336	ns
Tryp	0.2675	0.913	0.8336	ns
Tyr	0.2675	0.913	0.8336	ns
Val	0.2675	0.913	0.8336	ns

Supplementary Table 4